Shock Boundary Interactions Generated by the Fin on a Semi-cylindrical Body

Jiawei Sun[1]

1. Department of Mechanical and Aerospace Engineering, Tandon School of Engineering, New York University, Brookly, NY, USA.

Abstract

This study investigates the shock boundary layer interaction occurring at the base of a double sharp fin. The base geometry is of particular interest, with comparisons made between flat and semi-cylindrical bases. The flow field is characterized via numerical simulations and identifications of vortices in the flow field are made. There have been many studies on the shock boundary layer interaction generated by fins located on flat surfaces, but relatively few on fins located on semi-cylindrical surfaces.

It is observed in supersonic flow past a fin that the fluid in the contact region between the fin's root and the semi-cylinder exhibits turbulent phenomena, and the angle between the shock wave and the fin will decrease continuously as the Mach number increases. The separation shock will continuously move towards the fin root, and the vortex generated by the fin will reduce the speed of the fluid passing over the surface of the fin. After comparing separation vortices generated by plate-based fins and semi-cylinder fins, vortices generated by both the downwind fin and upwind fin rotate in the same direction in the semi-cylinder fin model, but separation vortices will change direction in downwind plate-based fin model. For the downwind plate-based fin, separation vortices will rise near the fin and descend far from the fin.

Further examination of the relationship between the Strouhal number and the Reynolds number will assist designers in predicting the behavior of aircraft under different speed conditions.

Nomenclature

M_{in}	Mach number of inlet
V_{in}	Velocity of inlet air
P_{in}	Pressure of inlet air
Re	Reynolds number based on momentum thickness
L	Sharp fin's length
H	Sharp fin's height
Δx	Average size of domain elements
δ	Thickness of the fin
α	Sharp fin half angle
x, y, z	Transverse, streamwise, spanwise coordinate axes
u, v, w	Transverse, streamwise, spanwise velocities

1 Introduction

Shock boundary interactions occur when supersonic flow go pass solid surface. The occurrence of this phenomenon has a negative impact on the stability of the aircraft. The shock boundary interaction and turbulence in the boundary layer greatly reduce the aircraft stability because the vortex will affect the stability of the inlet.

At the beginning of when researchers discovered the shock boundary interaction, people systematically studied the shock boundary interaction effect from a planar system. Arthur et al. conducted preliminary studies on shock waves and boundary layer thickness

near a plate by using pitot tubes and Töpler striation photographs [1]. Barry et al. presented oblique shock waves formed on a flat plate in supersonic fluids at Mach 2.0~2.5 using schlieren and interferometer photographs [2]. Yasuhara studied the supersonic flow past a flat plate with suction or injection, and found that the height and thickness of the boundary layer and the shock wave generated by the injection flow are greater than those of the suction [3].

At the same time, due to the negative effect of shock boundary interactions on the stability of the aircraft's intake, many studies had also been conducted on supersonic fluids inside inlet pipelines. Keenan et al. found through experimental testing that the apparent friction coefficient of compressible flows with equal Reynolds numbers and Mach numbers greater than or less than one is roughly equal to the friction coefficient of incompressible flows completely formed by the boundary layer [4]. Bershader et al. found that the shock waves generated by shock boundary interactions effect also exhibit an interferometric phenomenon [5]. Kaye et al. simplified many steps for the study of three-dimensional models by converting inlet pipeline models into one-dimensional model [6]. Studying supersonic flow in pipelines will help investigate the effects of supersonic flow passing over various surfaces.

On the basis of research [4-6], in order to further investigate the relationship between shock waves and geometric shapes, people began to study the flow of gas around simple geometric objects. Wachtell et al. studied supersonic flow in a tube with longitudinal slots [7]. Arnold et al. investigated cooled rough sphere's boundary layer transition in hypersonic flow [8].

The study of shock boundary interactions covers the establishment of simple two-dimensional and three-dimensional models. Based on research [7-8], in order to investigate the generation and characteristics of the shock wave and boundary layer turbulence, people took wings perpendicular to a smooth flat plate as the research object. In supersonic flow, the boundary layer of the shock wave generated by fins will run over the smooth flat plate it stands on, like the fin in Figure 1.1. Kim et al. investigated the turbulent thickness of the boundary layer in the lower hypersonic flow pass the plate, convex, and concave wedges using an experimental scheme using the interferometer and schlieren photography [9]. Fang et al. discovered the relationship between flow characteristics and wall turbulence, free shear layer turbulence, and corner vortex motion by studying single fins [10]. Wang et al. used fluid visualization methods such as nanoparticle based planar laser scanning to study the crossing shock wave/turbulent boundary layer interaction caused by double fins, and found that the boundary layer thickens behind the shock wave and converges towards the symmetry plate of the double fins [11]. Otten et al. found through their study of a 60deg leading edge sweep located on a flat plate at a Mach 2.5 flow field that the gap between fins and plates will change the position and shape of vortices generated by the leading edge of the fins [12]. Eitner et al. tested the physical phenomena of flexible materials in fluids with Mach number 2 using High speed stereoscopic digital image correlation and fast response pressure sensitive paint, and found that the fluid structure interaction is dominated by the large region of attached flow upwind of the base [13]. Zhou and others used fluid visualization to compare the area and intensity of separation vortices caused by curved and flat fins [14]. Zhao et al. also used a similar experimental setup to explore the impact free boundary layer interaction caused by curved fins [15]. Gang et al. found in their study on the turbulent separation behavior of blunt fins that when the sweep angle is less than 50 degrees, supersonic jets will form reflections on the surface of the fins [16]. Baldwin et al. found through fluid visualization that the interaction footprint is significantly influenced by Reynolds number, and this effect is more prominent at the interface between fins and surfaces and at the outer edge of the interaction area, which also provides inspiration for subsequent research [17].

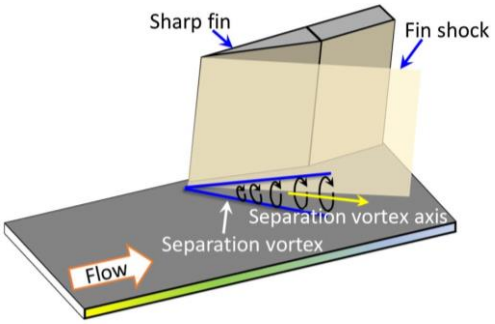

Figure 1.1: Shock boundary layer interactions generated by a sharp fin [18].

However, although a lot of time has been spent on the research of fin shape and angle of attack, people have overlooked the smooth plate on which the fins are based. Previous researches showed the shock wave generated by obstacles will generate friction between flow and the base smooth plate, resulting in turbulence in the boundary layer near it. Although there have been many studies on fins on smooth plates, there is still relatively little research on fins on semi-cylinders. In practical applications, shape of aircrafts designed by people is not entirely flat, and most of them are semi-cylinder or parabolic shape, so in practical applications, it is necessary to study the shock boundary interaction generated by fin over a curve surface or cylinder.

2. Numerical Settings

2.1 Geometry

The geometric design inspiration for this study comes from previous studies [18-20], which described shock boundary interactions generated by different fins. This semi-cylinder model spanned a full 180 deg and had an outer diameter of 25 cm. A boundary layer developed over the cylindrical surface that naturally transitioned to a turbulent boundary layer. A sharp fin with a leading-edge half-angle of 20 deg was mounted over the cylindrical surface at the middle of a semi-cylinder base. This fin was 25 cm tall, which is approximately a factor of four taller than the incoming boundary-layer thickness. The maximum thickness of the fin was approximately δ = 10 cm with the characteristic length L = 25 cm. The geometry of the cylinder and fin is shown in Figure 2.1.

Define the x-direction in geometry model as the transverse direction, the positive y-axis in geometry model as the streamwise direction, the z-axis in geometry model as the spanwise direction.

Orientation 1 in Figure 2.1a is facing the positive x-axis and located in downwind. Orientation 2 in Figure 2.1b is facing the positive direction of x-axis and located in upwind of the fin.

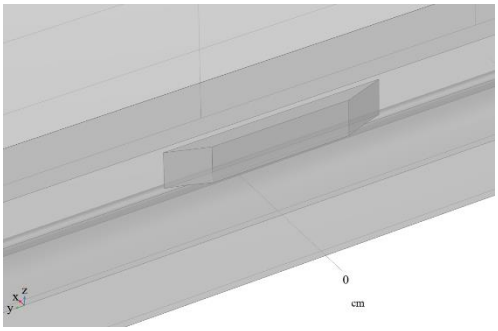

Figure 2.1a: Geometry of the cylinder and fin, orientation 1.

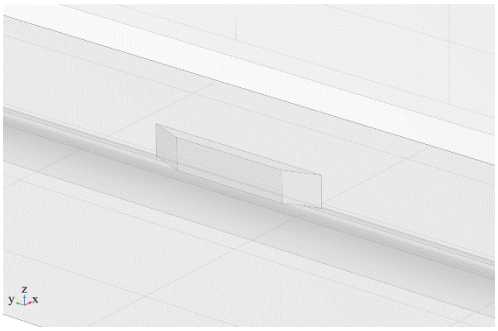

Figure 2.1b: Geometry of the cylinder and fin, orientation 2.

2.2 Physical Parameters

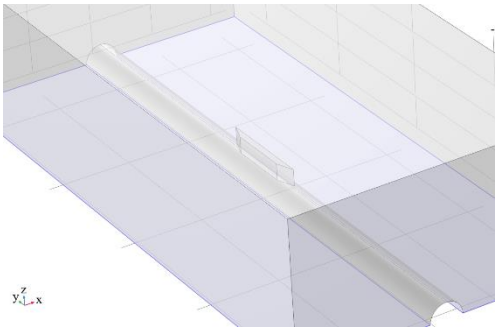

Figure 2.2: Geometry of the cylinder and fin, the blue plate is the base.

In the physical parameters of this paper, the model is to simulate the environment in open air, so each

boundary layer has special settings. Due to the fact that the boundary layer of this study is located at the contact part between the root of the fin and the cylinder, the blue plate in Figure 2.2 located at the bottom of the entire model (z = 0 cm) is defined as an open-air plate. Located on both sides, top, and tail of the model, it is defined as an exhaust port with equal pressure and an initial velocity of 0. The plate located at the upwind of the model is defined as an inlet with atmospheric pressure and an initial velocity of Mach 2 to Mach 3. All initial pressure values inside the calculation domain are set to atmospheric pressure, and the initial velocity value is set to the inlet velocity. This is a semi-cylinder model and its constant-area domain section is going to be define during calculation. Each run lasted 0.5 s, with a stagnation temperature of approximately 130 K and a constant stagnation pressure of 1 atm.

2.3 Domain and Meshing

In order to better determine the computational fluid domain, this research uses the length of the fin as the characteristic length L (150 cm). The computational fluid domain size is designed as an integer multiple of the characteristic length L, and whether it can fully include the entire fluid's influence area is the criterion for selecting this size. After determining the overall size of the fluid domain, $L/\Delta x$ will be used as an important indicator to determine the characteristic size of the computational fluid domain.

3 Numerical Methods

3.1 Governing Equations

The Navier-Stokes equations express mathematically the conservation of momentum and conservation of mass for a Newtonian fluid. They are accompanied by equations of state related to pressure, temperature, and density. The basic governing equations used in the simulations are the continuity equation, the momentum equation and the energy equation, where the density is variable. The detailed computational setup can be found in the paper:

Navier–Stokes equations:

Continuity equation:

$$\frac{\partial \rho}{\partial t} + \nabla \cdot (\rho V) = 0$$

Momentum equation:

$$\frac{\partial}{\partial t}(\rho V) + \nabla \cdot (\rho V \otimes V) = -\nabla p + \nabla \tau$$

Energy equation:

$$\rho \left[\frac{\partial y}{\partial x} + \nabla \cdot (hV)\right] = -\frac{Dp}{Dt} + \nabla \cdot (k \nabla T) + \Phi$$

General transport equations:

$$\frac{\partial}{\partial t}\int_V \rho\phi + \oint_A \rho\phi V dA = \oint_A \Gamma_\phi \nabla\phi dA + \int_V S_\phi dV$$

where

V is the fluid velocity vector.

τ is the viscous stress.

h is the enthalpy.

k is the thermal conductivity of the fluid.

Φ is the viscous dissipation.

Anderson (1995):

$$\frac{\partial}{\partial t}\vec{U} + \frac{\partial}{\partial x}\vec{X} + \frac{\partial}{\partial y}\vec{Y} + \frac{\partial}{\partial z}\vec{Z} = 0$$

$\vec{U}$, $\vec{X}$, $\vec{Y}$ and $\vec{Z}$ are defined as:

$$\vec{U} = \begin{bmatrix} \rho \\ \rho u \\ \rho v \\ \rho w \\ \rho E \end{bmatrix}$$

$$\vec{X} = \begin{bmatrix} \rho u \\ \rho u^2 + p - \tau_{xx} \\ \rho v u - \tau_{xy} \\ \rho w u - \tau_{xz} \\ \rho u E + p u - q_x - u\tau_{xx} - v\tau_{xy} - w\tau_{xz} \end{bmatrix}$$

$$\vec{Y} = \begin{bmatrix} \rho v \\ \rho u v - \tau_{yx} \\ \rho v^2 + p - \tau_{yy} \\ \rho w v - \tau_{yz} \\ \rho v E + p v - q_y - u\tau_{yx} - v\tau_{yy} - w\tau_{yz} \end{bmatrix}$$

$$\vec{Z} = \begin{bmatrix} \rho w \\ \rho u w - \tau_{zx} \\ \rho v w - \tau_{zy} \\ \rho w^2 + p - \tau_{zz} \\ \rho w E + p w - q_z - u\tau_{zx} - v\tau_{zy} - w\tau_{zz} \end{bmatrix}$$

τ is viscous stress tensor. *X*, *Y* and *Z* are the called the flux terms, and the solution vector is *U*.

3.2 Algorithms

The determination of calculation domain and mesh grid will provide a foundation for subsequent computational simulations. In this study, the *high Mach number flow* of Comsol Multiphysics was used to simulate the fin and the surrounding environment, which uses finite element volume to solve the Navier-Stokes equations in three-dimensional steady-state compressible flows.

The relative tolerance, difference between the results of every two simulations, is set to 0.005, and the calculation will only start and stop when this tolerance is reached. The maximum number of iterations is set to 15000 times.

The scheme is set as using PARDISO linear solver for calculating the flow field. PARDISO is a software for solving large sparse symmetric or structurally symmetric linear systems of equations on shared memory multiprocessors. PARDISO combines left- and right-looking Level-3 BLAS supernode techniques to exploit pipelining parallelism [23]. PARDISO discretizes continuous physical problems into a set of linear equations using the finite element method, and then establishes a linear system. PARDISO gradually approximates the solution through an iterative process.

To complete the Strouhal number and obtain the frequency of vortex shedding, the simulation software Comsol usually uses the transient solver with the implicit backward differentiation formula, because its solving process is more stable. This method is based on linear multi-step techniques, approximating the derivative of the function by using the function values determined in the time direction [21, 22]. Discretize the Navier-Stokes equations in space using finite element method, and then apply backward differentiation formula to discretize the time derivatives in the ODEs. Backward differentiation formula approximates the time derivative at the current time step using values from previous time steps.

Backward difference in 1st derivative representations is:

$$\left(\frac{\partial f}{\partial x}\right)_{i,j} = \frac{f_{i+1,j} - f_{i,j}}{\Delta x} + O(\Delta x)$$

where

$x_{i,j}$ are grid points, and $\left(\frac{\partial f}{\partial x}\right)_{i,j}$ is first derivative term.

And backward difference in 2nd derivative representations is:

$$\left(\frac{\partial^2 f}{\partial x^2}\right)_{i,j} = \frac{f_{i,j} - 2f_{i-1,j} + f_{i-2,j}}{(\Delta x)^2} + O(\Delta x)$$

where

$\left(\frac{\partial^2 f}{\partial x^2}\right)_{i,j}$ is second derivative term.

4 Computational Results

4.1 Domain Size and Grid Density

To ensure the size of the computational fluid domain will not affect the final calculation result, the size of the domain must be large enough to include all fluids affected by the fin. The height of the computational fluid domain is set to *a*L*, the width is set to *b*L*, and the length is set to *c*L*, shown in Figure 4.1 (*a*, *b*, and *c* are random natural numbers). Therefore, taking the fin as the center, select three straight lines in *x*, *y*, and *z* direction and record the pressure ratio at the current position to inlet pressure (P/P_{in}) on these three straight lines:

Transverse: $\begin{cases} y = 0\ cm \\ z = 37.5\ cm \end{cases}$ where *y* is located in the center of fin and *z* is located in the midpoint of fin height.

Streamwise: $\begin{cases} x = -15\ cm \\ z = -25\ cm \end{cases}$ where *x*-distance from the fin is δ and *z* is located in the root of the fin.

Spanwise: $\begin{cases} x = -40\ cm \\ y = 0\ cm \end{cases}$ where this line is located between the bottom half cylinder and domain's wall.

The reason for choosing these three lines is that they are all located near the shock waves caused by the

fin, which can cover more influence area of shock waves generated by the fin.

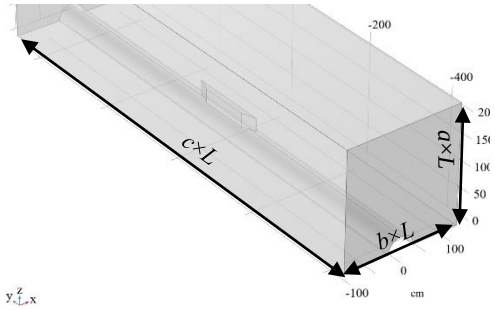

Figure 4.1: Computational fluid domain.

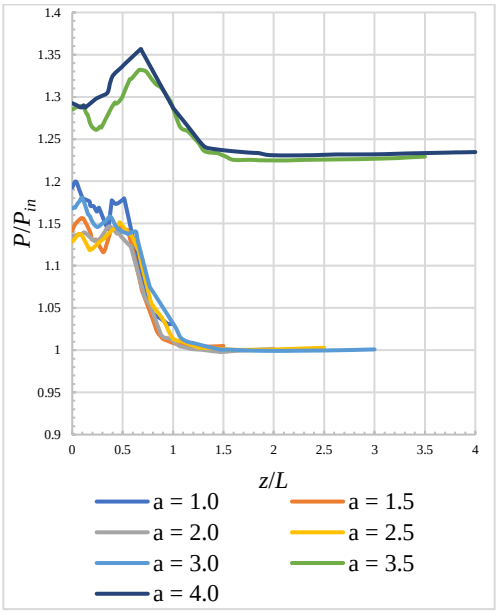

Figure 4.2a: Spanwise pressure distribution (M_{in} = 2.0).

To ensure that all fluid area affected by the fin are included, calculation domain must include pressure changes at each location. Therefore, the most important feature is that boundaries of the computational fluid domain must be far enough away from the fin, which is

$$\lim_{x/L \to boundary} \frac{P}{P_{in}} = 1$$

According to Figure 4.2a, in the spanwise, take the bottom of entire computational domain as the starting point and the top of the domain as the endpoint. As the length of the computational domain in the spanwise increases from 1.5 L to 3.0 L, the pressure ratio P/P_{in} approaches 1 successively and then no longer increases. However, when the computational domain is too large, such as when the length of the domain in the spanwise is 3.5 L or 4.0 L (when a = 3.5 and 4.0 in Figure 4.2a), whole pressure ratio P/P_{in} is higher than 1, which means the entire computation becomes distorted. The area where the fin cause disturbance to the fluid is only up to 1.5 L, which means in the selection of domain size in this direction, the length in the spanwise should only be 1.5 L. Similarly, the size of the computational fluid domain should be 3 L in the transverse and 6 L in the streamwise. Here is the result of the domain's size:

$$\begin{cases} a = 1.5 \\ b = 3 \\ c = 6 \end{cases}$$

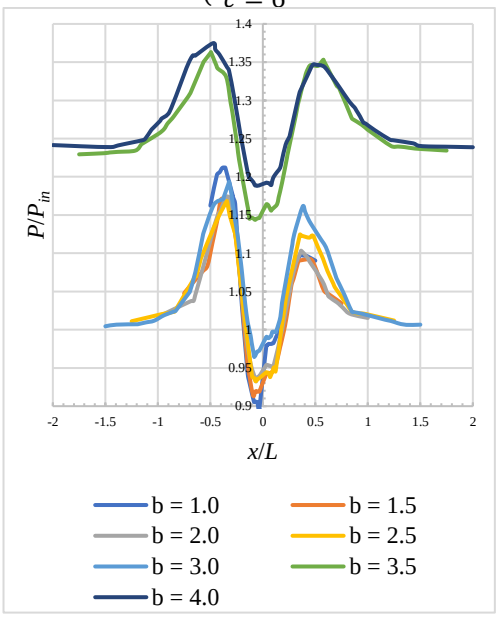

Figure 4.2b: Transverse pressure distribution (M_{in} = 2.0).

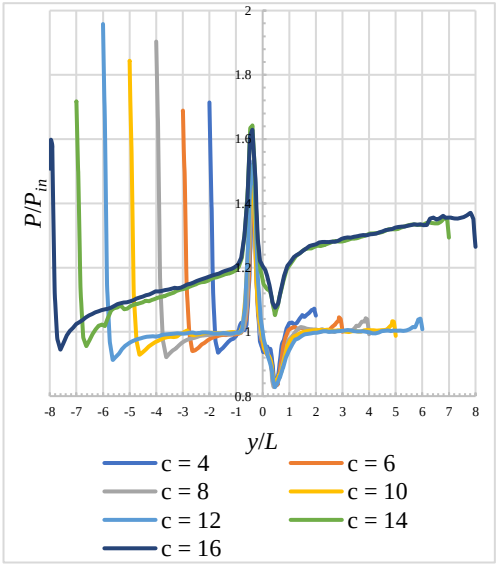

Figure 4.2c: Streamwise pressure distribution (M_{in} = 2.0).

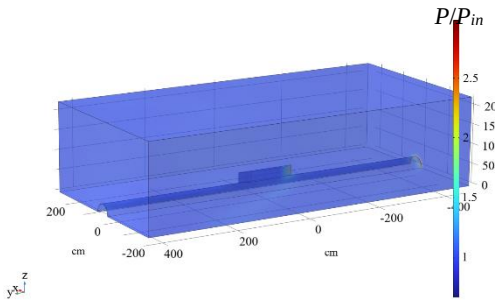

Figure 4.3: Global map of pressure ratio for the entire domain.

The light blue part in Figure 4.3 indicates that the pressure inside the domain will not be affected by the size of the domain, including that the domain is sufficiently large.

Based on calculating domain density Δx, take a transverse straight line at y = -75 cm (fin's tip) and z = 37.5 cm (fin's height midpoint), and record the pressure change curves under different grid sizes in Figure 4.4. According to this figure, when the grid density is too high, the stability of numerical calculations in simulation results decreases, leading to significant round-off error. The lengths of each unit grid are similar ($\Delta x = \Delta y = \Delta z$). Therefore, in this case, choosing a grid density of $L/\Delta x$ = 87.72 is the best choice.

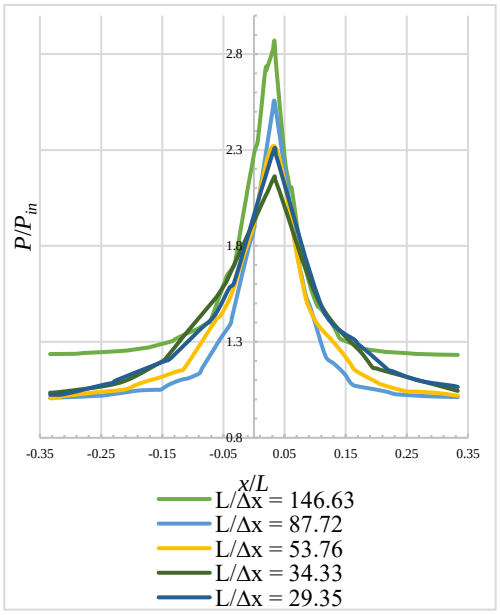

Figure 4.4: Transverse pressure distribution (M_{in} = 2.0).

4.2 Characterization of the Flow Field around Upwind Fin

4.2.1 Velocity Field

Take a plate parallel to the base and record the data on it in Figure 4.6 (z = 25 cm), and take another red plate (Figure 4.5a and 4.5d) in the position of y = -63.81 cm. Due to the fluid flow being directed along the negative y-axis, and the velocity u in the transverse being perpendicular to the direction of the intake, a high slope of velocity in the transverse indicates a shockwave in the fluid. The separation vortex (show in Figure 4.6) generated by the fin located on the half cylinder is located in separation vortex of the figure. In Figure 4.6, 4.5c, and 4.5f, dark blue represents the flow moving along the negative z-axis direction (spanwise), while red and yellow represent the flow moving along the positive z-axis direction (spanwise). The appearance of flow with completely opposite directions in the same region confirms the existence of the separation vortex, and the direction of the vortex is shown in Figure 4.5c and 4.5f. In Figure 4.6, the separation vortex rises from the side near the fin and descends from the side away from the fin. In Figure 4.5c and 4.5f, the lower boundary of the separation vortex is almost tightly attached to the base and extends outward along the base, regardless of whether the base is flat or semi-cylindrical. Figure 4.5b only shows the separation vortex generated by fin and base plate. Figure 4.5e shows the separated flow generated by fin on a semi-cylindrical body. On the left side of the fin in Figure 4.5b and Figure 4.5e, the light blue part at the connection of two dark blue areas shows a significant decrease in transverse velocity, as that is where the separation shock is located.

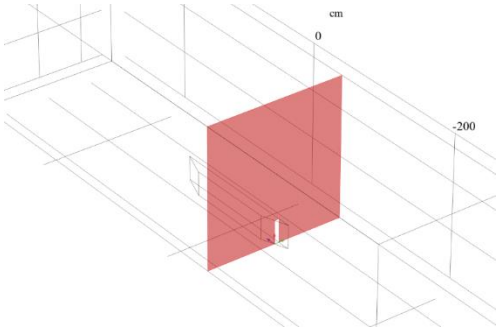

Figure 4.5a: Geometric plate (red plate) for Figure 4.5b.

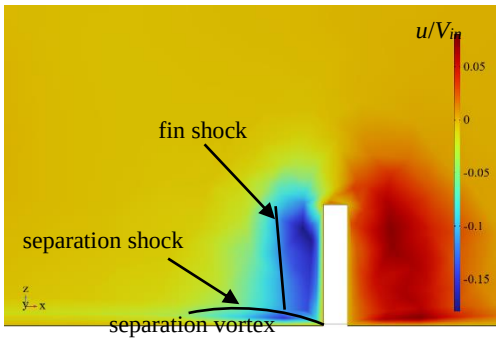

Figure 4.5b: Transverse velocity distribution generated by the fin on plate (M_{in} = 3.0).

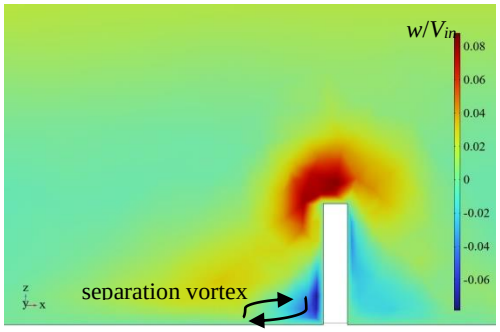

Figure 4.5c: Spanwise velocity distribution generated by the fin on plate (M_{in} = 3.0).

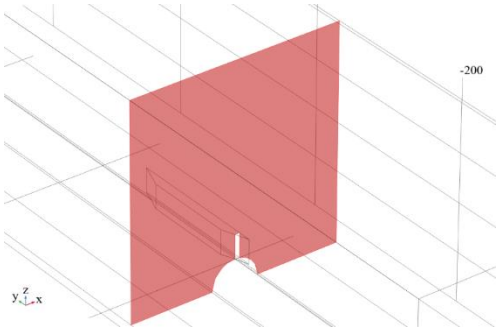

Figure 4.5d: Geometric plate (red plate) for Figure 4.5e.

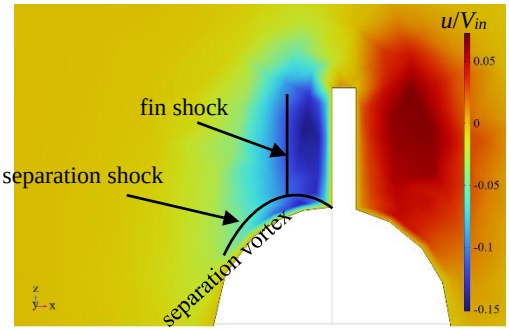

Figure 4.5e: Transverse velocity distribution generated by the fin on cylinder (M_{in} = 3.0).

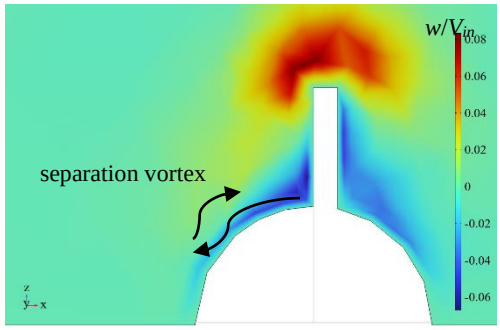

Figure 4.5f: Spanwise velocity distribution generated by the fin on cylinder (M_{in} = 3.0).

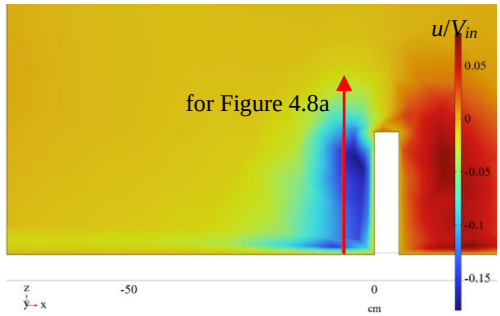

Figure 4.5g: Numerical sampling lines (red) for Figure 4.8 (M_{in} = 3.0).

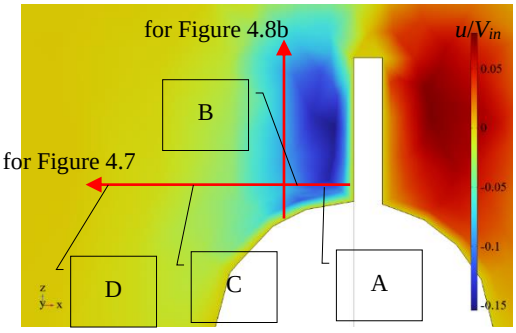

Figure 4.5h: Numerical sampling lines (red) for Figure 4.7 and 4.8 (M_{in} = 3.0).

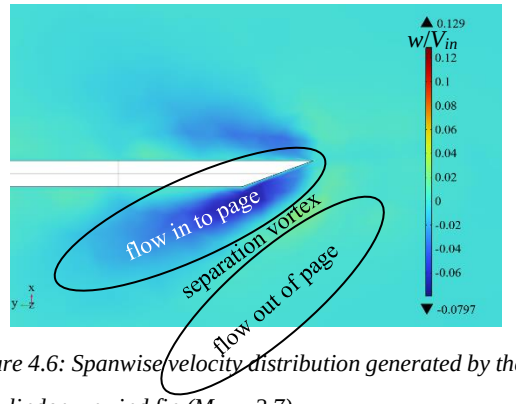

Figure 4.6: Spanwise velocity distribution generated by the fin on cylinder, upwind fin (M_{in} = 2.7).

The area transitioning from blue to yellow and from red to yellow in Figure 4.5b and 4.5e are both boundaries of shock waves, and vortex is between two shock boundaries. The difference between plate-based fin and cylindrical-based fin is that because the separation shock is closely attached to the base, the separation shock on the half cylinder gradually extends to the bottom of the half cylinder, while the separation shock on the flat plate is closely adjacent to the flat plate until the boundary of domain. In practical design, due to the fact that the surface of many aircraft with fins is not completely flat, the separation vortex and separation shocks generated by fins will spread along the surface of the aircraft, rather than spreading as in flat experiments. However, from Figure 4.5b and 4.5e, there is no difference between the two in terms of vortices size, and there is no significant change in the thickness of the boundary layer.

On the cross-section of the Figure 4.5b and 4.5e, the presentation of many data points remains unclear; therefore, the subsequent data analysis is based on the data of the red line in the cross-section of Figure 4.5g and 4.5h. Take a straight line perpendicular to the fin as the data collection point for Figure 4.7. The direction indicated by the arrow in Figure 4.5h is the positive direction of the horizontal axis. This dataset measured the relationship between the ratio of the transverse velocity to the inlet velocity and the distance from the bottom, as the varies M_{in} from 2.0 to 3.0. Select four points in Figure 4.7 and correspond them to Figure 4.5h. For the data in Figure 4.7, in the horizontal direction, the transverse velocity reaches its maximum approximately 0.45 δ from the tip of the fin (point A), gradually decreasing until it diminishes to zero at a distance of 3.8 δ (point D). Notably, there is a significant decrease in transverse velocity at approximately 0.75 δ to 2.4 δ (point B to point C), suggesting the feasibility of defining this point as the "fin shock". Subsequent data analysis focuses on the region located at a distance of 0.75 δ from the tip of the fin.

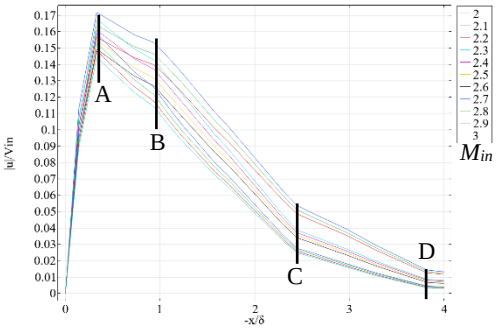

Figure 4.7: Transverse velocity distribution generated by the fin on cylinder.

In Figure 4.7, the slope of u/V_{in} has changed at point B. From Figure 4.5h, it can be observed that point B is the intersection point between the fin shock and the separation shock. This is the reason for u/V_{in}'s slope changed at point B. Similarly, at point C, the shock generated by the fin will continue to move horizontally, while the separation shock generated by the semi-cylindrical base will move downwards outside the measurement area, resulting in a sudden change in u/V_{in}. It is worth noting that the u/V_{in} slope between AB is similar to that between CD, as between AB and CD, the u/V_{in} slope is only related to the shock generated by the fin.

Take a straight line parallel to the left side of the fin at a distance of 0.75 δ as the data collection point for Figure 4.8a and 4.8b. The direction indicated by the arrow in Figure 4.5h is the positive direction of the horizontal axis. Starting from the bottom of the straight line, record the ratio of the fluid velocity u/V_{in} in the transverse to the inlet flow velocity from bottom to top. In Figure 4.8a and 4.8b, regardless of whether the bottom

is a flat plate or a half cylinder, the transverse velocity reaches its peak at approximately 0.06 *H* and then decreases to 0.2 *H*. Therefore, it can be considered that the thickness of the separation shock boundary is equal and all are 0.2 *H*. As the height gradually rises to the top of the fin, the transverse velocity slowly increases between 0.2 *H* and 0.8 *H*. Therefore, it can be observed that there is a second shock boundary on the upper part of the fin, and the center of this fin shock boundary in Figure 4.8a is located at 0.8 *H*, and shock boundary in Figure 4.8b is located at 0.75 *H*.

Furthermore, it can be seen that the difference between Figure 4.8a and Figure 4.8b lies in the position of the peak of transverse velocity. The results indicate that the shock boundary at the endpoint in Figure 4.8a is higher than that in Figure 4.8b, indicating that the fin shock's boundary generated by the fin on the flat plate at the *z*-axis position is higher than that on the fin on the half cylinder.

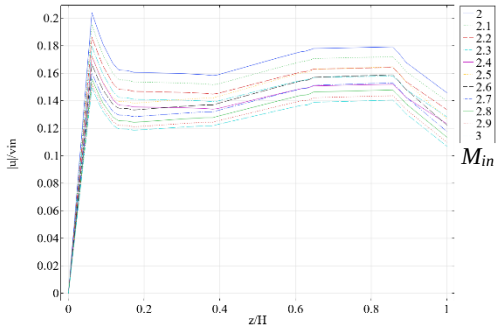

Figure 4.8a: Transverse velocity distribution (fin on flat plate).

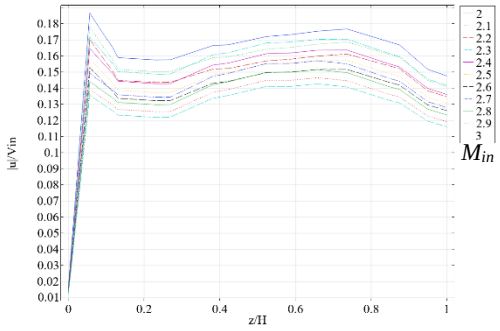

Figure 4.8b: Transverse velocity distribution (fin on cylinder).

4.2.2 Pressure Field

In Figure 4.9, the fluid enters the domain along the positive *y*-axis and collides with the fin to form a shock wave. The shock wave presents an umbrella shaped shape in Figure 4.9, with the umbrella tip facing opposite to the direction of the intake (negative *y*-axis direction). There is a small high-pressure area (P/P_{in} = 3.1) in the area where the fin faces the fluid in Figure 4.9f. Similarly, there is a low-pressure area (P/P_{in} = 0.71) at the tail of the fin. After comparing Figures 4.9a-4.9b, 4.9c-4.9d, and 4.9e-4.9f, it can be observed that the pressure changes next to the fin are similar, whether on a flat plate or a half cylinder, when subjected to air impact at the same flow rate. Except for the interference of the lower semi-cylinder on the fluid, the influence of the fin themselves at the flow is not significantly different. The outside is blue or purple because the pressure ratio P/P_{in} of the outside does not change much. From Figure 4.9f, the pressure ratio P/P_{in} at the tip of the fin is the highest.

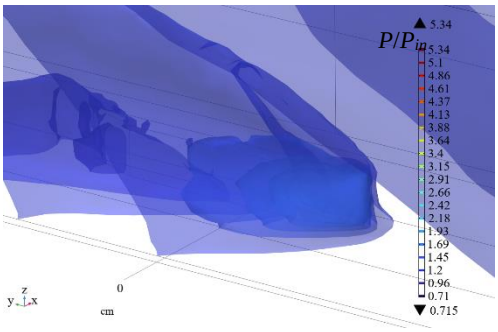

Figure 4.9a: Pressure contours, orientation in Figure 2.1b (fin on plate) (M_{in} = 3.0).

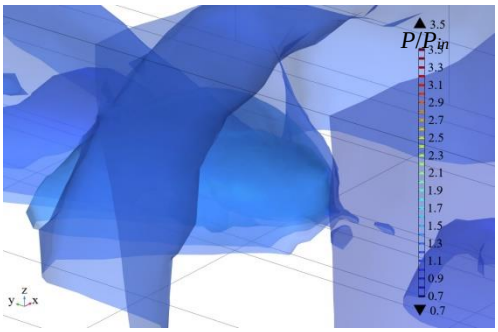

Figure 4.9b: Pressure contours, orientation in Figure 2.1b (fin on cylinder) (M_{in} = 3.0).

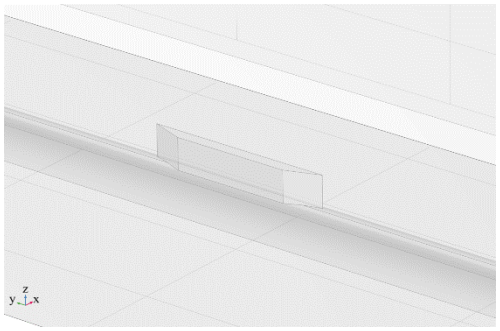

A copy of Figure 2.1b, for the orientation of Figure 4.9b.

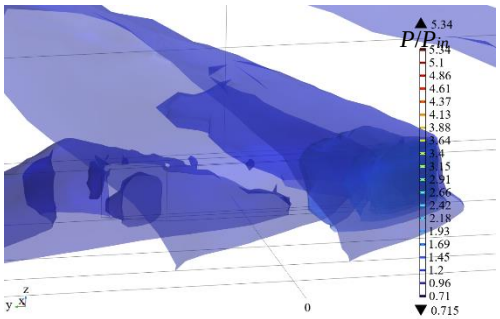

Figure 4.9c: Pressure contours, orientation in Figure 2.1c (fin on plate) (M_{in} = 3.0).

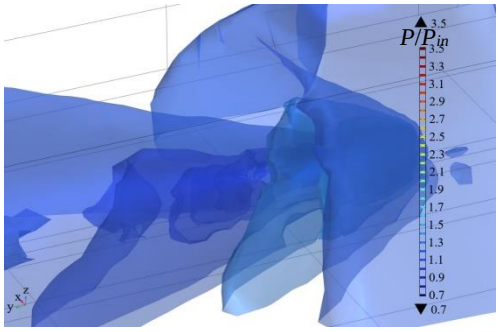

Figure 4.9d: Pressure contours, orientation in Figure 2.1c (fin on cylinder) (M_{in} = 3.0).

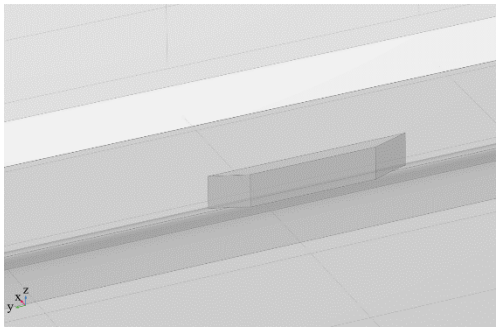

A copy of Figure 2.1c, for the orientation of Figure 4.9d.

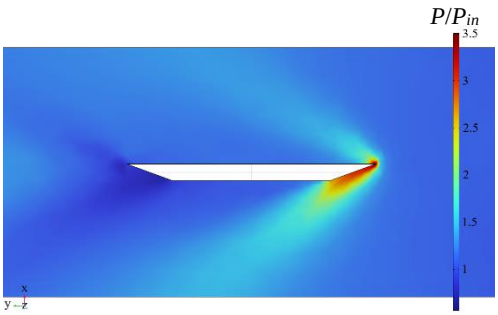

Figure 4.9e: Pressure contours on the horizontal slice at the root of the fin (fin on plate) (M_{in} = 3.0).

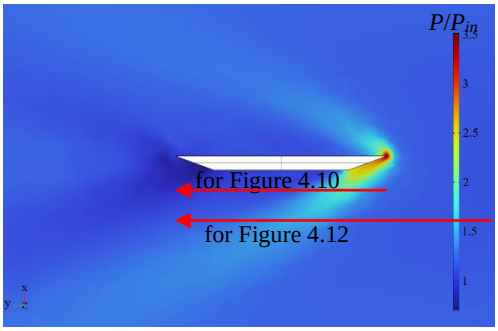

Figure 4.9f: Pressure contours on the horizontal slice at the root of the fin (fin on cylinder) (M_{in} = 3.0).

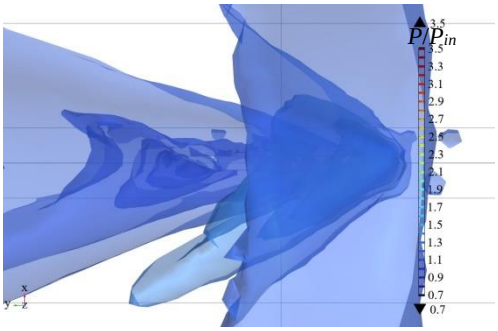

Figure 4.9g: Pressure contours throughout the entire domain, orientation in Figure 4.9f (fin on cylinder) (M_{in} = 3.0).

In order to analyze the pressure changes of the fluid on the surface of the fin, take a line with a distance to fin in 2 δ with a length of L, and record the pressure change at each point to Figure 4.10 for further analyze. The direction indicated by the arrow in Figure 4.9f is the positive direction of the horizontal axis. The following two sets of figures were drawn with the streamwise y/L value as the x-axis and the ratio of surface pressure to inlet pressure P/P_{in} as the y-axis.

In Figure 4.10, it can be observed that the peak pressure appears around y/L = 0.25, corresponding to the high-pressure area on the right side of Figure 4.9d. The lowest pressure value appears when the pressure near the fin is y/L = 1, corresponding to the low-pressure area on the left side in Figure 4.9d. The higher the inlet flow velocity, the higher the average pressure around the fin.

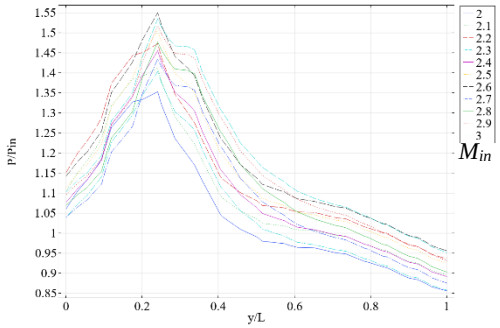

Figure 4.10: Pressure variation along a line that one 2 δ away from the fin.

4.3 Variation of Separation Shocks' Angle

In Figure 4.10, the position of the peak pressure undergoes a sudden change at a certain moment. In order to explore the angle changes of separation shocks, the Mach number contour surface can more intuitively display the angle of separation shocks.

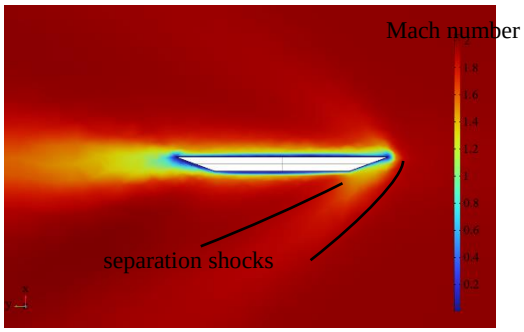

Figure 4.11a: Separation shocks and Mach number contour surface on the horizontal slice at the root of the fin (fin on cylinder) (M_{in} = 2.0).

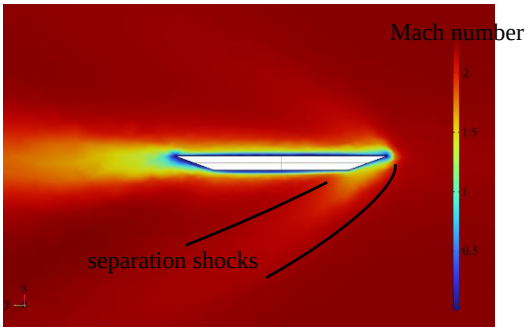

Figure 4.11b: Separation shocks and Mach number contour surface on the horizontal slice at the root of the fin (fin on cylinder) (M_{in} = 2.3).

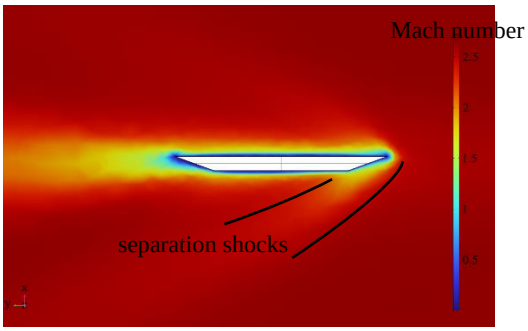

Figure 4.11c: Separation shocks and Mach number contour surface on the horizontal slice at the root of the fin (fin on cylinder) (M_{in} = 2.7).

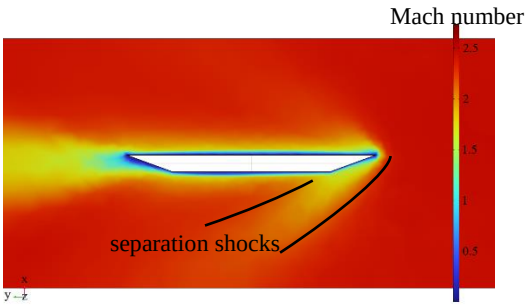

Figure 4.11d: Separation shocks and Mach number contour surface on the horizontal slice at the root of the fin (fin on plate) (M_{in} = 2.7).

After comparing Figure 4.11a, 4.11b, and 4.11c, it can be observed that the angle between separation shocks and the sharp fin significantly decreases when the Mach number jumps from 2.0 to 2.7. Moreover, the width of entire separation shock has also decreased significantly. Also, comparing Figures 4.11c and 4.11d, it can be observed that when the Mach numbers passing

through the fin are the same, the position and direction of the two separation shocks are the same, regardless of whether the fin is on a plane or a semi-cylinder.

Take a group of straight lines parallel to the fin with a distance to fin in 0.5 δ, δ, 2 δ, 3 δ, 4 δ, with a length of 2 L and analyze the Mach number on that line and recording these data for Figure 4.12 to analyze position of separation shocks. The direction indicated by the arrow in Figure 4.9f is the positive direction of the horizontal axis. Define the positive x-axis as the positive direction of the fluid, and the y-axis as the Mach number.

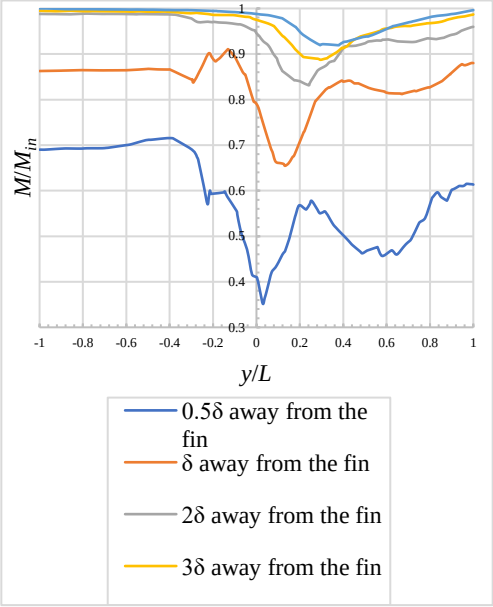

Figure 4.12a: Change in Mach number along the parallel line with the fin (M_{in} = 2.0).

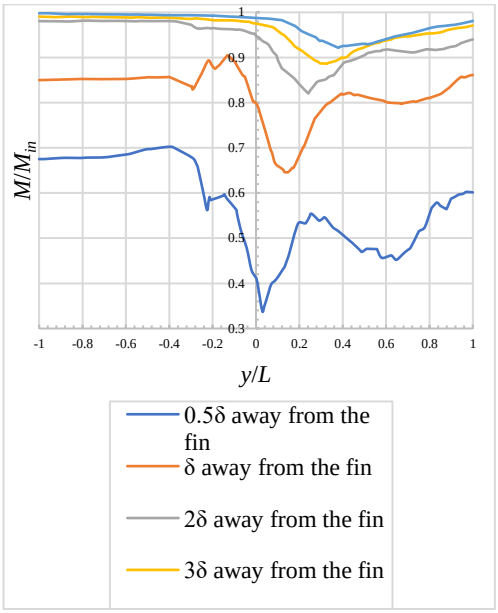

Figure 4.12b: Change in Mach number along the parallel line with the fin (M_{in} = 2.3).

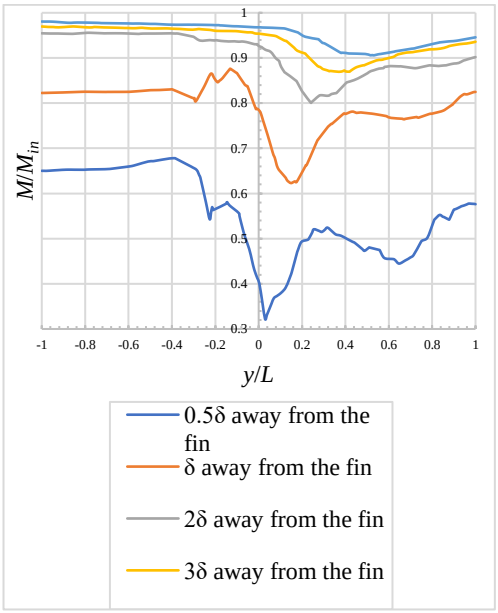

Figure 4.12c: Change in Mach number along the parallel line with the fin (M_{in} = 2.7).

When the Mach number is less than or equal to 2.4, the Mach number valley appears at about 0.2 L, and the thickness is about 0.1 L. When the Mach number is greater than or equal to 2.5, the Mach number valley appears at approximately 0.25 L. The valley value of each M/M_{in} is the influence area of the separation shock. Based on Figure 4.12, by comparing the positions of the valleys in each group of data, the positional changes of

the two separated shocks in Figure 4.11 can be verified. Similarly, it can be observed that as the Mach number increases from 2.0 to 2.7, not only does the angle between separated shocks and the fin decrease, but also the distance between two separation shocks also becomes narrow.

4.4 Strouhal Number in High Reynolds Number Flow

All experiments were simulated by Comsol at a Reynolds number from 2.8E5 to 2.8E6. Measuring the relationship between Strouhal number and Reynolds number can reveal the shedding frequency of vortices at different Reynolds numbers and their relationship with fluid dynamics characteristics. This helps to study the formation, evolution, and flow stability of vortices.

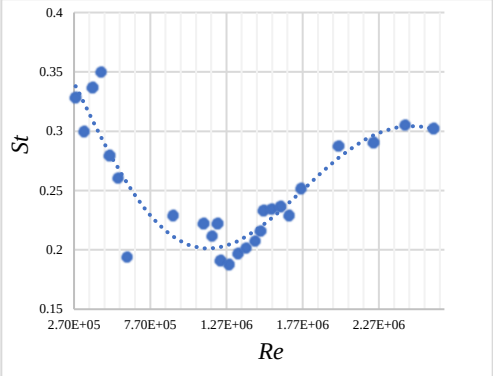

Figure 4.13: St vs Re in 20 deg fin.

Figure 4.13 is the result of combining these three sets of data. According to the image, it can be observed that the relationship between Strouhal number and Reynolds number generally follows the following pattern. In Figure 4.13, solid points represent experimental data, while dashed lines represent trend curves fitted by the data set using the least squares method.

When Reynolds number is higher than 1.27E6, the flow becomes more turbulent, the frequency of vortex shedding increases, leading to an increase in Strouhal number.

Secondly, in a certain range of high Mach number fluids, the formation and shedding of vortices are influenced by various factors and may exhibit periodic changes, thus exhibiting certain periodic characteristics. As the Reynolds number steadily increases, the Strouhal number does not steadily increase, but first decreases and then increases.

Finally, according to the data integration in Figure 4.13, it can be found that the relationship between Strouhal number and Reynolds number may reflect the stability characteristics of the flow. When the Reynolds number is in an area (around 1.27E6), the flow may be in a turbulent state but the Strouhal number is small; when the Reynolds number is high, the flow may become more turbulent and the Strouhal number may increase.

4.6 Velocity Field of the Flow around the whole Fin

In Figure 4.14a, a separation shock will be generated at both the upwind and upwind fin, and the difference is that the shock waves generated by the upwind fin are compressed waves, and shock waves generated by the downwind fin are expansion waves. In Figure 4.14c, there are also two separation shocks similar to Figure 4.11.

Consistent with the phenomenon observed in Chapter 4.3, the shape of the fin base does not significantly alter separation shocks and surrounding pressure generated by the fin.

However, after comparing Figures 4.11e and 4.11f, it can be observed that the direction of the vortices generated at the tail of the fin has been changed.

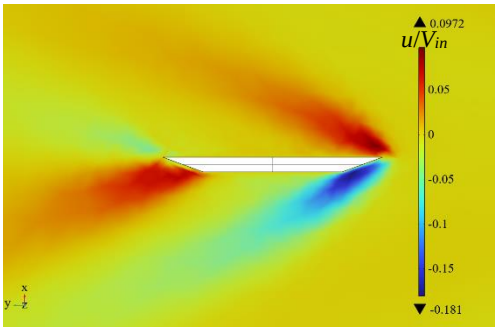

Figure 4.14a: Transverse velocity contour surface on the horizontal slice at the root of the fin (fin on cylinder) (M_{in} = 2.7).

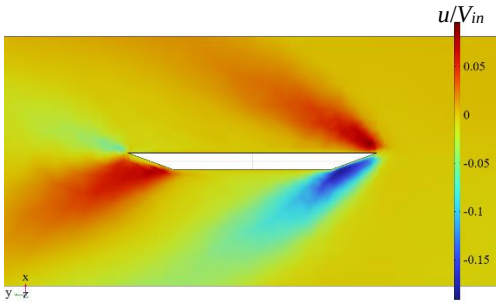

Figure 4.14b: Transverse velocity contour surface on the horizontal slice at the root of the fin (fin on plate) (M_{in} = 2.7).

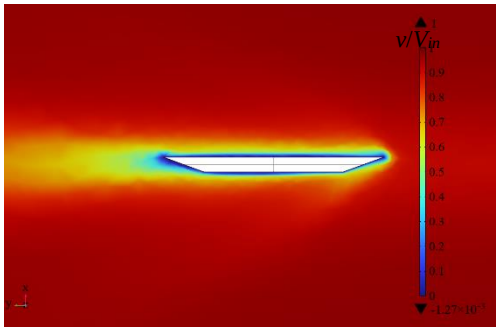

Figure 4.14c: Streamwise velocity contour surface on the horizontal slice at the root of the fin (fin on cylinder) (M_{in} = 2.7).

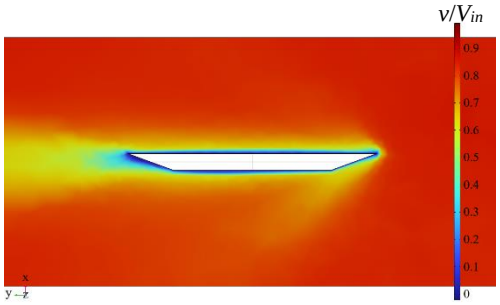

Figure 4.14d: Streamwise velocity contour surface on the horizontal slice at the root of the fin (fin on plate) (M_{in} = 2.7).

Figure 4.14e, which shows the fin based on semi-cylinder, includes four separation vortices, two are generated by the upwind fin and two are generated by the downwind fin, similar to the separation vortex in Figure 4.6. It is worth noting that the vortex direction caused by the downwind fin is exactly the same as that caused by the upwind fin. In two separation vortices generated by the downwind fin, the vortex rises far away from the fin and descends near the fin.

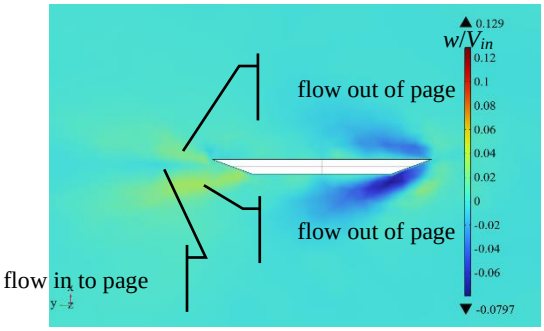

Figure 4.14e: Spanwise velocity contour surface on the horizontal slice at the root of the fin (fin on cylinder) (M_{in} = 2.7).

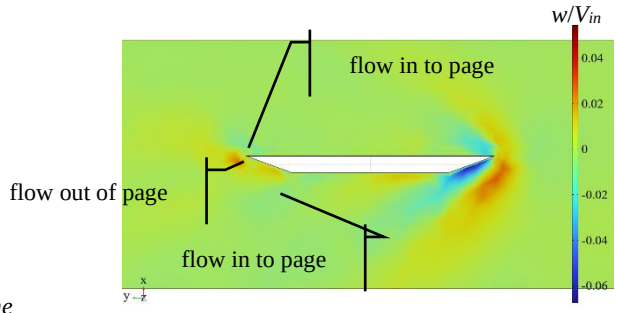

Figure 4.14f: Spanwise velocity contour surface on the horizontal slice at the root of the fin (fin on plate) (M_{in} = 2.7).

In Figure 4.14f, which shows the fin based on plate, four separated vortices can be seen, but the rotation direction of separation vortices generated by the downwind fin is completely opposite to that generated by the upwind fin. The separation vortices generated by the downstream fin rise near the fin and descend in the direction away from the fin.

5 Conclusion and Future Works

When the supersonic fluid passes over the fin on semi-cylinder, it will inevitably generate a vortex between the root of the fin and its base, and this vortex can reduce the speed of the surface fluid passing over the fin in a certain area. Moreover, whether it is a downwind or an upwind fin on semi-cylinder, the direction of vortex rotation generated by it is consistent: falling near the fin and rising far away the fin. However, when the fin is located on a plate, the rotation direction of separation vortices near the downwind fin reverses, and the cause of this phenomenon is currently unclear.

At the same time, the shock wave generated by the fin shock boundary interaction will be changed in accordance with the change of the fin's base. This implies that during the actual design process of an aircraft, the shock wave generated by fin-shaped objects will traverse the fuselage, and impact any entity it encounters.

The Strouhal number and Reynolds number of the vortex generated by the supersonic fluid passing over the fin are not a simple linear relationship. Specific situations still need to be discussed in future experiments.

In the follow-up work, there are still many new studies need to be carried out in order to further determine the shock wave of the base on the shock wave and the design location of the hypothetical air intake. In addition, in order to further ensure the stability of the air intake, the study of the vortex frequency generated by different shapes of fins and bases is also needed. Meanwhile, studying the rotation direction of separation vortices will be a crucial task: Investigating why the shape of the base of the downwind fin can change the rotation direction of separation vortices.

Reference

[1] Fage, A., & Sargent, R. F. (1947). Shock-wave and boundary-layer phenomena near a flat surface. Proceedings of the Royal Society of London. Series A, Mathematical and Physical Sciences, 190(1020), 1–20. https://doi.org/10.1098/rspa.1947.0058.

[2] Barry, F. W., Shapiro, A. H., & Neumann, E. P. (1950). Some Experiments on the Interaction of Shock Waves With Boundary Layers on a Flat Plate. Journal of Applied Mechanics, 17(2), 126–131. https://doi.org/10.1115/1.4010089.

[3] Yasuhara Michiru. (1957). On the Hypersonic Viscous Flow past a Flat Plate with Suction or Injection. Journal of the Physical Society of Japan, 12(2), 177–182.

[4] Keenan, J. H., & Neumann, E. P. (1946). Measurements of Friction in a Pipe for Subsonic and Supersonic Flow of Air. Journal of Applied Mechanics, 13(2), A91–A100. https://doi.org/10.1115/1.4009532.

[5] Bershader, D. (1949). An Interferometric Study of Supersonic Channel Flow. Review of Scientific Instruments, 20(4), 260–275. https://doi.org/10.1063/1.1741506.

[6] Kaye, J., Keenan, J. H., Klingensmith, K. K., Ketchum, G. M., & Toong, T. Y. (1952). Measurement of Recovery Factors and Friction Coefficients for Supersonic Flow of Air in a Tube: 1—Apparatus, Data, and Results Based on a Simple One-Dimensional Flow Model. Journal of Applied Mechanics, 19(1), 77–96. https://doi.org/10.1115/1.4010410.

[7] Wachtell, G. P., & Carfagno, S. P. (1959). Supersonic Flow in a Tube with Longitudinal Slots. The Physics of Fluids (1958), 2(5), 521–526. https://doi.org/10.1063/1.1705943.

[8] Kuethe, A. M., Ishii, T., & Amick, J. L. (1964). Boundary-Layer Transition on a Cooled Rough Sphere in Hypersonic Flow. The Physics of Fluids (1958), 7(8), 1198–1200. https://doi.org/10.1063/1.1711361.

[9] Kim, C.-S. (1959). Experimental Studies on the Hypersonic Flow past Plate, Convex and Concave Wedges. Journal of the Physical Society of Japan, 14(6), 827–837. https://doi.org/10.1143/JPSJ.14.727.

[10] Fang, J., Yao, Y., Zheltovodov, A. A., & Lu, L. (2017). Investigation of Three-Dimensional Shock Wave/Turbulent-Boundary-Layer Interaction Initiated by a Single Fin. AIAA Journal, 55(2), 509–523. https://doi.org/10.2514/1.J055283.

[11] Wang, L., Zhao, Y., Wang, Q., Zhao, Y., Zhang, R., & Ma, L. (2022). Three-dimensional characteristics of crossing shock wave/turbulent boundary layer interaction in a double fin with and without micro-ramp control. AIP Advances, 12(9), 095309-095309–095314. https://doi.org/10.1063/5.0102986.

[12] Otten, D. L., & Lu, F. K. (2022). Flow features of swept shock/turbulent boundary-layer interaction due to

a gap beneath a sharp fin. Aerospace Science and Technology, 130, 107934-.
https://doi.org/10.1016/j.ast.2022.107934.

[13] Eitner, M. A., Ahn, Y.-J., Musta, M. N., Clemens, N. T., & Sirohi, J. (2023). Vibration of a thin panel exposed to ramp-induced shock-boundary layer interaction at Mach 2. Journal of Fluids and Structures, 119, 103894-.
https://doi.org/10.1016/j.jfluidstructs.2023.103894.

[14] Zhou, Y. Y., Zhao, Y. L., He, G., Zhao, Y. X., & Gao, P. Y. (2023). Study on the separation in the shock wave/boundary layer interaction induced by a curved fin. Physics of Fluids (1994), 35(7). https://doi.org/10.1063/5.0155076.

[15] Y. Zhao, Y. Zhou, G. He and Y. Zhao. (2023). Visualization of shock-free compression/laminar boundary layer interaction caused by a curved fin in supersonic flow, 17th Asian Congress of Fluid Mechanics (ACFM 2023), 24-29, doi: 10.1049/icp.2023.1924.

[16] GANG, D., YI, S., ZHANG, F., & NIU, H. (2022). Effects of sweep angles on turbulent separation behaviors induced by blunt fin. Chinese Journal of Aeronautics, 35(3), 90–97.
https://doi.org/10.1016/j.cja.2021.03.032.

[17] Baldwin, A., Mears, L. J., Kumar, R., & Alvi, F. S. (2021). Effects of Reynolds Number on Swept Shock-Wave/Boundary-Layer Interactions. AIAA Journal, 59(10), 3883–3899.
https://doi.org/10.2514/1.J060293.

[18] Pickles, J. D., & Narayanaswamy, V. (2020). Control of Fin Shock Induced Flow Separation Using Vortex Generators. AIAA Journal, 58(11), 4794–4806. https://doi.org/10.2514/1.J059624.

[19] McCormick, D. C. (1993). Shock/boundary-layer interaction control with vortex generators and passive cavity. AIAA Journal, 31(1), 91–96. https://doi.org/10.2514/3.11323.

[20] Gaitonde, D. V., & Adler, M. C. (2023). Dynamics of Three-Dimensional Shock-Wave/Boundary-Layer Interactions. Annual Review of Fluid Mechanics, 55(1), 291–321. https://doi.org/10.1146/annurev-fluid-120720-022542.

[21] Bruno, O. P., Cubillos, M., & Jimenez, E. (2019). Higher-order implicit-explicit multi-domain compressible Navier-Stokes solvers. Journal of Computational Physics, 391, 322–346. https://doi.org/10.1016/j.jcp.2019.02.033.

[22] Nived, M. R., Athkuri, S. S. C., & Eswaran, V. (2022). On the application of higher-order Backward Difference (BDF) methods for computing turbulent flows. Computers & Mathematics with Applications (1987), 117, 299–311. https://doi.org/10.1016/j.camwa.2022.05.007.

[23] Schenk, O., Gärtner, K., Fichtner, W., & Stricker, A. (2001). PARDISO: a high-performance serial and parallel sparse linear solver in semiconductor device simulation. Future Generation Computer Systems, 18(1), 69–78. https://doi.org/10.1016/S0167-739X(00)00076-5.

Acknowledgements

I appreciate my parents and families for their support, both mentally and financially. Also, I am grateful for my mentor Dr. Nicholas DiZinno (industry professor in NYU Tandon) for providing me with academic guidance.